Additive Manufacturing 67 (2023) 103478

Contents lists available at ScienceDirect

Additive Manufacturing

journal homepage: www.elsevier.com/locate/addma

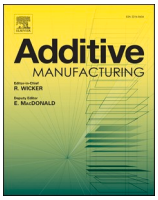

Strengthening additively manufactured Inconel 718 through in-situ formation of nanocarbides and silicides

Emre Tekoğlu [a,1], Alexander D. O'Brien [a,1], Jian Liu [b,1], Baoming Wang [c], Sina Kavak [d], Yong Zhang [c], So Yeon Kim [c], Shitong Wang [a], Duygu Ağaoğulları [d,e], Wen Chen [b,*], A. John Hart [f,*], Ju Li [a,c,**]

[a] Department of Nuclear Science and Engineering, Massachusetts Institute of Technology, Cambridge 02139, USA
[b] Department of Mechanical and Industrial Engineering, University of Massachusetts, Amherst 01003, USA
[c] Department of Materials Science and Engineering, Massachusetts Institute of Technology, Cambridge 02129, USA
[d] Particulate Materials Laboratories, Metallurgical and Materials Engineering Department, Istanbul Technical University, Maslak, Istanbul 34469, Turkey
[e] Istanbul Technical University, Prof. Dr. Adnan Tekin Materials Science and Production Technologies Applied Research Center (ATARC), Maslak, Istanbul 34469, Turkey
[f] Department of Mechanical Engineering, Massachusetts Institute of Technology, Cambridge 02139, USA

ARTICLE INFO

Keywords:
Laser powder bed fusion
Ni-based superalloy
Additive manufacturing
Mechanical property
In-situ alloying

ABSTRACT

We report additive manufacturing (AM) of a nickel superalloy metallic matrix composite (Ni-MMC) using laser powder bed fusion (LPBF). Nanoceramic-containing composite powders were prepared by high-speed blender declustering and ball milling of as-received SiC nanowires (2 vol%) and Inconel 718 alloy powders, which produced a homogeneous decoration of SiC on the surfaces of Inconel particles. Analysis of the as-printed specimens revealed the dissolution of SiC nanowires during laser melting, leading to the in-situ formation of Nb- and Ti-based silicide and carbide nanoparticles. These in-situ formed nanoparticles resulted in a more desirable solidification microstructure of the AM Inconel 718 with fewer printing defects (cracks and pores) and slightly refined grain sizes. Mechanical characterization of the as-printed Ni-MMCs revealed notable increases in hardness, yield strength (by 16%), and ultimate tensile strength (σ_{UTS}, by 12%) compared to the reference samples without SiC addition. After heat treatment, the same composite samples displayed a 10% higher σ_{UTS} compared to identically treated unreinforced material while maintaining ~14% total tensile elongation. We believe this in-situ precipitate formation presents a simple and effective method for strengthening additively manufactured high-temperature materials that could be used in the increasingly harsh environments in energy and propulsion applications.

1. Introduction

Inconel 718 is a class of a gamma double prime (γ'') Ni-Cr superalloy precipitation-hardened through aging treatment, which, owing to its superior high-temperature creep and fatigue resistance in combination with excellent oxidation resistance, is a staple among materials for applications in extreme conditions [1–3]. Inconel series alloys at large are widely utilized in aerospace, aviation, and nuclear industries, which require high endurance under extreme chemical and thermomechanical conditions [3,4]. As technology improves, however, further increasing performance in these applications will require operation at even higher temperatures and stresses, pushing beyond the limits of the current superalloys. With this in mind, the research community has witnessed a significant focus in recent years on developing techniques for further improving the capabilities of Inconel alloys.

One such technique is ceramic reinforcement, resulting in Inconel-based metal matrix composites (MMCs). By implanting ceramic fibers or particles into the Inconel matrix, researchers are able to tailor grain size and morphology, reinforce grain boundaries, and, in some cases, achieve improved high-temperature mechanical properties [5–9].

* Corresponding authors.
** Corresponding author at: Department of Nuclear Science and Engineering, Massachusetts Institute of Technology, Cambridge 02139, USA.
E-mail addresses: wenchen@umass.edu (W. Chen), ajhart@mit.edu (A.J. Hart), liju@mit.edu (J. Li).
[1] These authors contributed equally to this work.

https://doi.org/10.1016/j.addma.2023.103478
Received 14 November 2022; Received in revised form 5 February 2023; Accepted 1 March 2023
Available online 2 March 2023

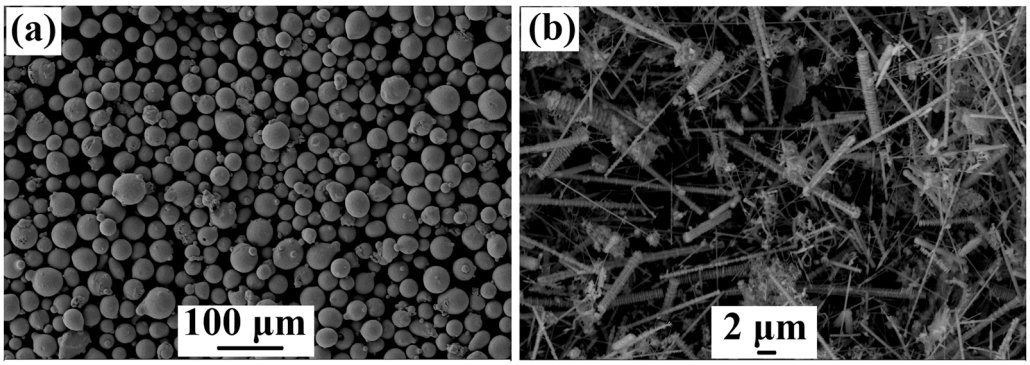

Fig. 1. SEM images of raw powders utilized for MMC fabrication. (a) Inconel 718 and (b) SiC_{nw}.

Table 1
Chemical composition of Inconel 718 pristine powders, which is measured by EDX.

Element	Ni	Fe	Cr	Nb	Mo	Ti	Co	Al	Mn
wt%	52.5	19.9	17.2	4.8	2.9	0.9	0.9	0.8	0.1

Metal-bases such as Al, Cu, Fe, and Ti have been utilized to improve the mechanical and thermal properties of structural components [10]. While the strengthening effects associated with these MMCs are highly desirable, traditional manufacturing methods have frequently proven inadequate for the production of high-quality composites, especially for the notoriously difficult-to-manufacture nickel alloys. MMCs prepared through casting processes typically suffer from poor wettability of the ceramic nano-fillers and inhomogeneous distribution in the liquid metal matrix [11–13]. Further, traditional powder metallurgy methods require high-cost molds for compacting powders and remain incapable of producing parts with sought-after complex geometries (lattice structures, inner coolant ducts, etc.) [14–18]. Due to the difficulties with traditional manufacturing methods, additive manufacturing (AM) techniques such as powder bed fusion (PBF) and directed energy deposition (DED) are potential approaches to producing Inconel-based MMCs, which enable the production of unique and difficult-to-manufacture complex geometries [19,20]. PBF technologies, including Electron Beam Melting (EBM) and Laser Powder Bed Fusion (LPBF), provide many advantages, such as weight reduction, low buy-to-fly ratios, high level of customization, simplified supply chains, and reduced need for joining and assemblies in comparison to conventional manufacturing routes [21–23]. Moreover, PBF technologies can lead to higher dimensional accuracy and better feature resolution compared to other AM processes [23–27]. Therefore, the integration of MMC material groups with PBF manufacturing techniques is considered to be a highly promising route for components made of new high-temperature alloys.

The mechanical performance of additively manufactured nickel MMCs still has significant knowledge gaps [28]. In the current literature, several studies have examined PBF production of carbide or boride particle reinforced Inconel MMC materials, especially with regards to samples reinforced with TiC or TiB_2 and produced via LPBF [29–31]. In one such study, Gu et al. [31] produced 10 wt% TiC reinforced Inconel 718 (In718) composite powders by ball milling and fabricated bulk composite samples from these powders via LPBF. The as-printed In718–10 wt% TiC achieved 4.5 GPa hardness, around 18% higher than that of unreinforced In718 alloy produced through the same technique. In another study, Mandal et al. [30] fabricated reinforced In718 composites by LPBF with varying concentrations of TiC (0, 10, 20 and 30 wt%). Microhardness results showed that the hardness of the 30 wt% TiC reinforced In718 composites increased by 78% compared to the unreinforced In718 printed at the same LPBF conditions. Regarding bulk mechanical properties, Yao et al. [32] produced 2 wt% nano-TiC reinforced In718 powders through ball milling. The LPBF as-printed composites showed higher yield strength (σ_y, 774 versus 647 MPa) and ultimate tensile strength (σ_{UTS}, 1029 versus 940 MPa) than the pure In718 samples. However, after standard heat treatment (HT) to produce the gamma prime (γ') and gamma double prime (γ'') precipitates, σ_y and σ_{UTS} of the Inconel 718 – 2 wt% TiC became lower than the unreinforced Inconel 718 alloys (1144 versus 1211 MPa, 1381 versus 1408 MPa), with a significantly lower elongation (9% versus 15%) [32], showing a degradation of tensile properties.

Here, we present results from LPBF of an In718-based MMC reinforced by the addition of SiC nanowires. SiC represents a promising additive for MMCs due to its superior hardness and strength at elevated temperatures as well as good oxidation and thermal resistance [33,34], but to our knowledge, it has not been explored as a reinforcing agent in In718. In this study, 2 vol% SiC-nanowire (SiC_{nw}) reinforced In718 (hereinafter denoted as In718+SiC) composite powders were prepared via high-speed blending followed by ball milling. Bulk specimens of unreinforced In718 and In718+SiC composites were fabricated via LPBF using a commercial 3D printer (EOS M290). These printed specimens were subjected to a standard three-step heat treatment to mimic an industry standard processing of In718 parts [35], following which both the heat-treated (HT) and as-printed samples with and without SiC were analyzed by electron microscopy and X-ray diffraction to assess the developed grain structures and phases. Further, we quantified the average microhardness and tensile strength of each of the four sets of materials, which revealed strengthening (σ_{UTS}, 1527 versus 1398 MPa) with good maintenance of uniform tensile ductility, with much improved total tensile elongation (14%) compared to previous work on TiC-reinforced In718 [32]. We believe that this work positively impacts the current research on nickel MMCs by expanding the library of reinforcing materials and by introducing a new composite that specifically achieves among the best combinations of post-heat treatment tensile strength and ductility yet reported. More importantly, this work provides a new straightforward and scalable avenue for strengthening laser additively manufactured alloys, producing reinforcing carbides and silicides via in-situ chemical reactions, which is expected to have great potential for expansion to new MMCs and application to industries seeking improved high-temperature structural components.

2. Materials and methods

2.1. Powder preparation

For this study, the base metal matrix was gas atomized In718 series alloy powder with particle diameters of 15–45 μm (MSE Supplies LLC, Tuczon, AZ, USA). Reinforcing ceramic nanomaterials consisted of SiC nanowires of 99% purity featuring wire lengths of 50–100 μm and diameters 0.1–0.6 μm (Sinet Advanced Materials Co., Ltd, China). SEM images of the initial powders pre-mixing are provided in Fig. 1. SEM images confirm that the particle size distributions (PSD) are compatible

Table 2
Printing parameters utilized in LPBF.

Laser power (W)	285
Scanning speed (mm/s)	960
Layer thickness (μm)	40
Hatch spacing (μm)	110
Laser spot size (μm)	100
Scan rotation (°)	67
Volumetric energy density (J/mm^3)	67.47
Build plate preheating temperature (°C)	80
Shield gas and its purity	Ar, 99.9%
Build plate material	4140 steel

with the specifications provided by powder suppliers. Additionally, Table 1 shows the chemical composition of the pristine Inconel 718 powders as measured by EDX.

2 vol% SiC_{nw} were mixed with In718 powders in batches of 500 g in a high-speed blender (VM0104, Vita-Mix, USA) for 90 min in order to decluster the nanowires and mix them as single strands with the In718 powders. Afterwards, In718+SiC powders were split into batches and ball milled for 30 min in a Pulverisette 7 planetary micro mill (Fritsch, Idar-Oberstein, Germany) at 600 rpm. Stainless steel vials (80 ml) and balls (diameter 5 mm) were utilized with a ball-to-powder weight ratio of 5/1. 99.5% stearic acid (MilliporeSigma, Burlington, MA, USA) was added to the powders at 2 wt% as a process control agent to prevent cold welding to the vials and agglomeration of particles during milling. Milling vials with sealed gassing lids to maintain an inert atmosphere were loaded and unloaded in a glove box under 99.999% purity argon (Linde, Marlborough, MA, USA) to prevent surface contamination and oxidation of the powders. Stearic acid was removed from ball-milled composite powders in a furnace at 420 °C for 2 h under argon.

2.2. Laser powder bed fusion

As-purchased unreinforced In718 powders and ball-milled 2 vol% SiC_{nw} reinforced In718 composite powders were printed via LPBF using a commercial system (EOS M290). Table 2 provides the printing

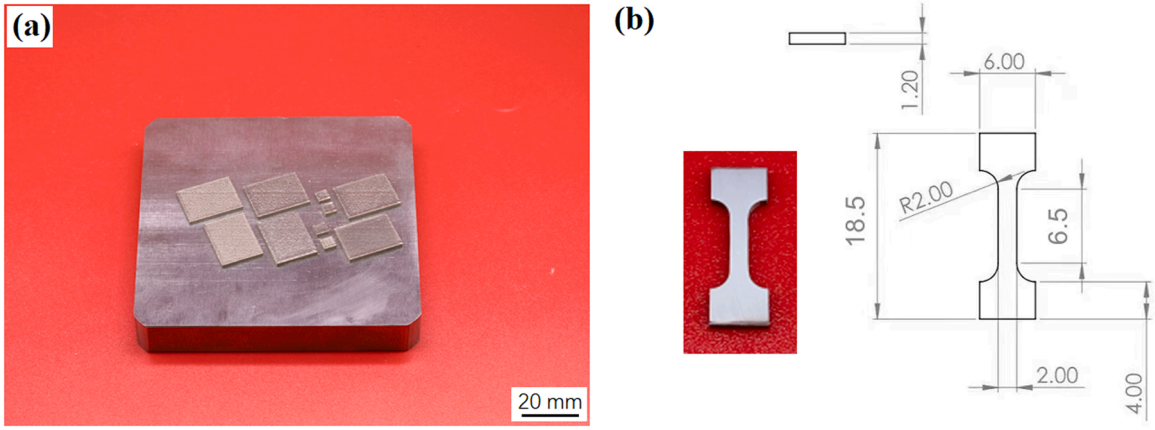

Fig. 2. (a) In718–2 vol% SiC_{nw} samples fabricated using EOS M290 LPBF printer and (b) A representative tensile specimen machined by wire EDM and specimen dimensions.

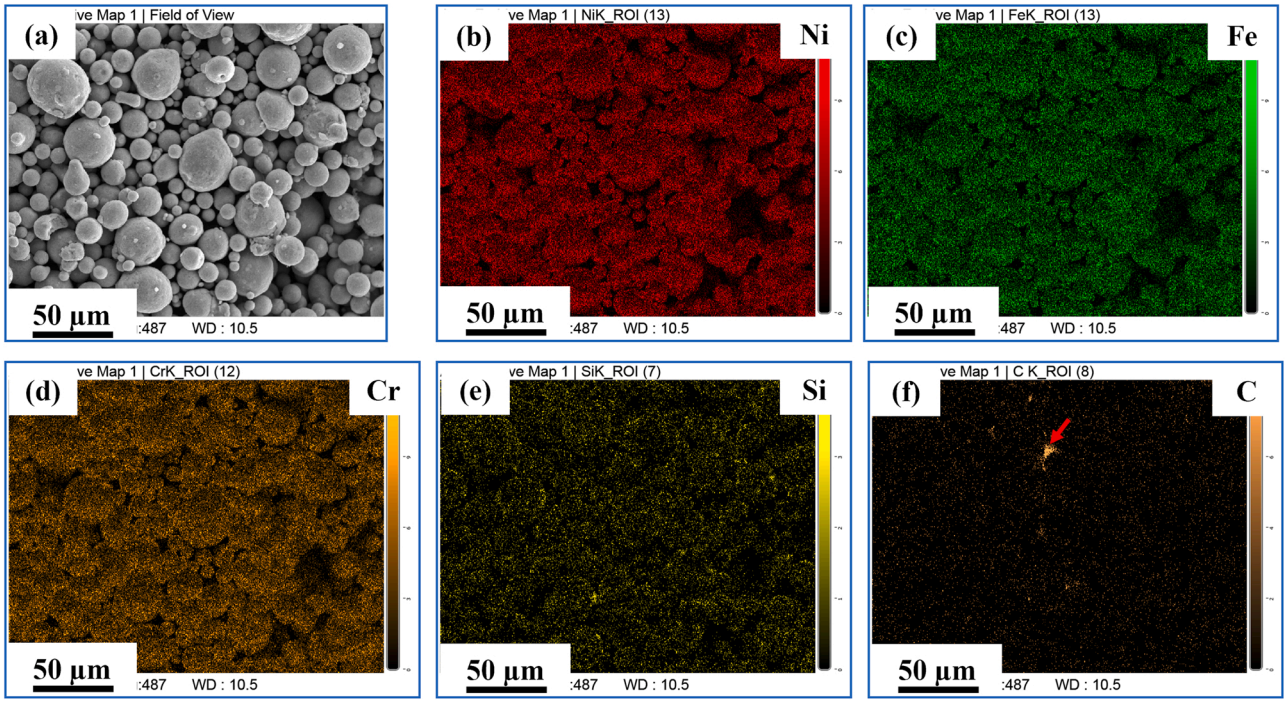

Fig. 3. SEM images and EDX mappings obtained from In718+SiC powders following declustering and ball milling.

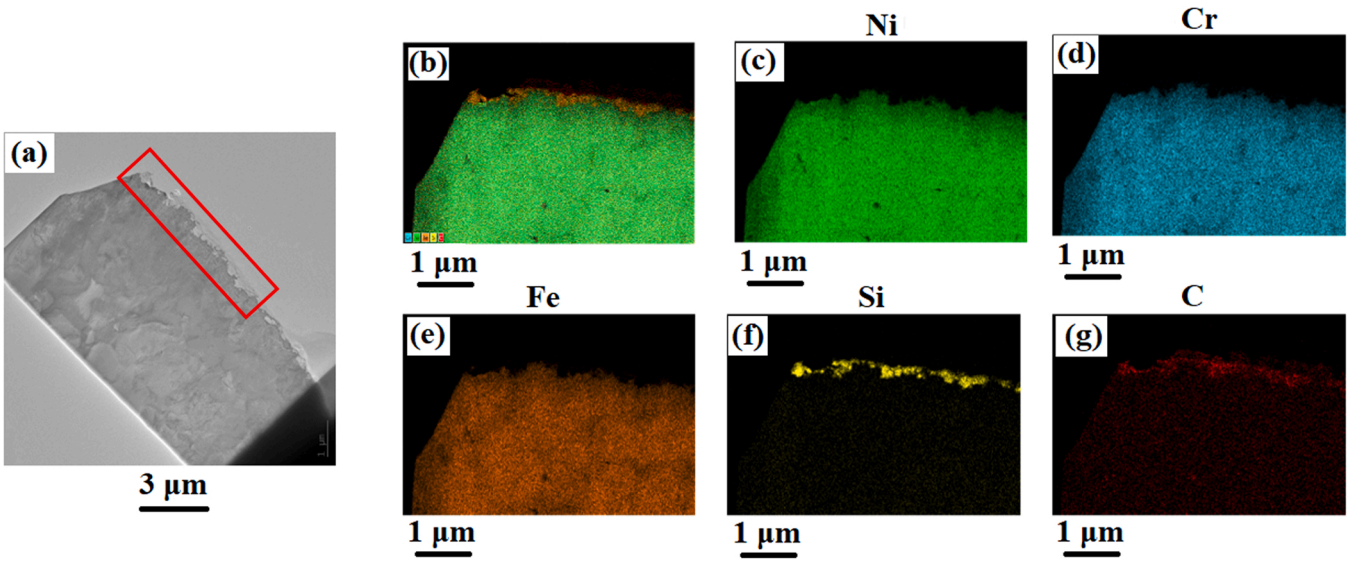

Fig. 4. (a) TEM image, (b) composite EDX mapping, and (c-g) individual element EDX mapping results obtained from the cross-section of a single SiC-coated In718 particle following ball milling.

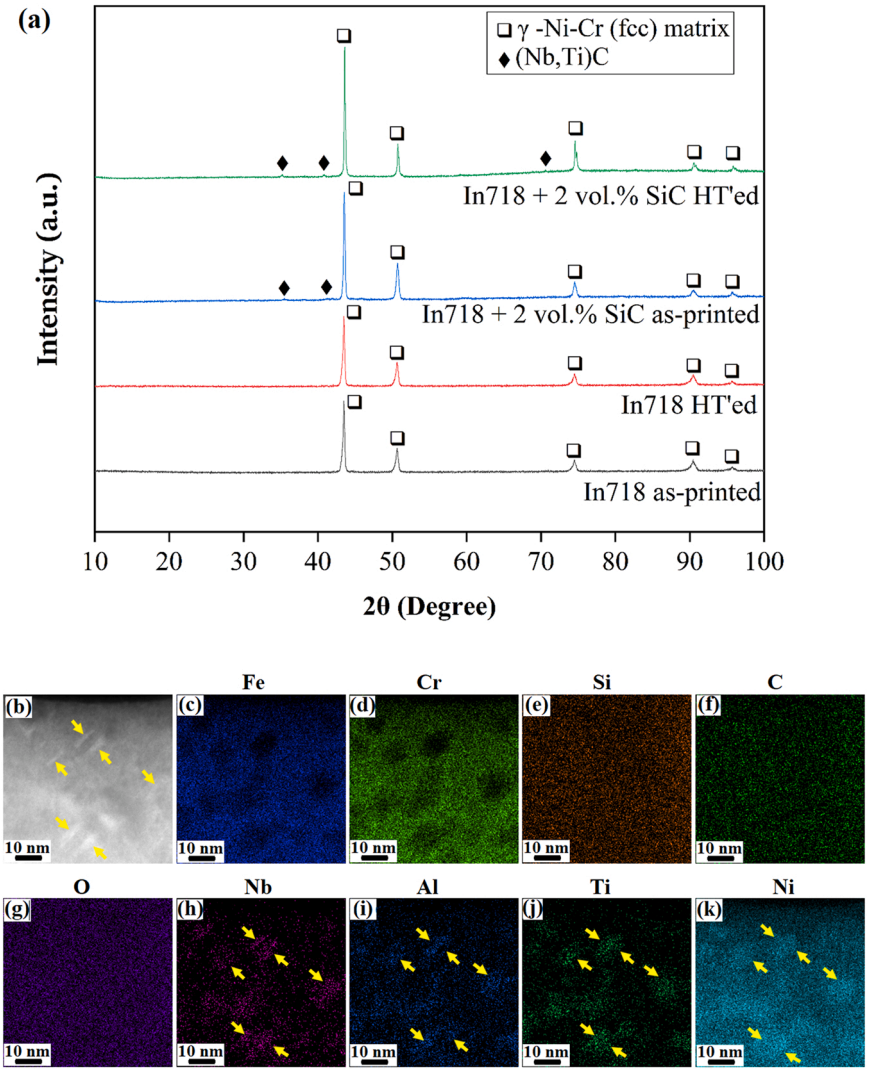

Fig. 5. **(a)** XRD analysis obtained from In718 and In718+SiC with and without HT, and **(b-k)** STEM image and corresponding EDX mapping analysis obtained from HT'ed In718+SiC sample revealing the precipitates within the In718 matrix.

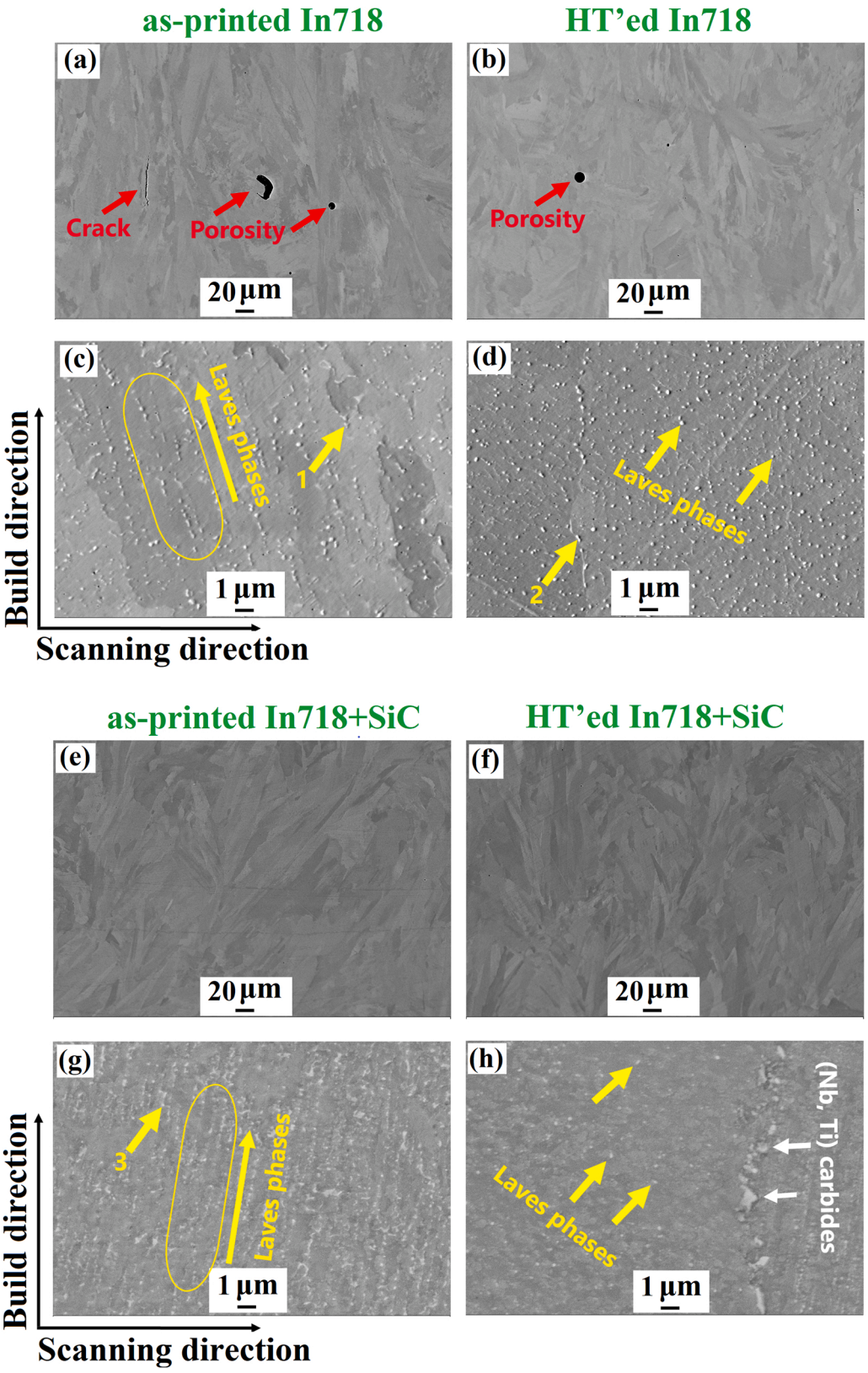

Fig. 6. Secondary electron SEM images obtained from: (a, c) as-printed In718, (b, d) HT'ed In718, (e, g) as-printed In718+SiC and (f, h) HT'ed In718+SiC. The samples are cut along the build direction.

Table 3
EDX Analysis of points 1–5 from Fig. 6.

	Point 1	Point 2	Point 3	Point 4	Point 5	General EDS obtained from as-printed In718+SiC
Ni	43.65	41.07	41.79	42.66	6.96	52.83
Fe	16.68	18.82	17.83	18.64	1.32	19.21
Cr	15.85	18.11	18.48	18.77	1.54	16.94
Nb	10.84	10.24	10.71	9.62	60.32	4.27
Ti	1.17	1.31	1.69	1.39	17.86	0.76
Al	0.84	0.77	0.81	0.97	1.03	0.87
Mn	-	-	-	-	0.12	0.17
Si	1.31	0.94	0.87	1.41	0.27	0.31
C	1.64	1.7	-	-	10.21	2.21
Mo	8.02	7.04	7.82	6.54	0.37	2.43

parameters applied to all samples. These parameter sets were determined based on data from previously published LPBF studies of In718 [36–39]. Fig. 2(a) displays the In718+SiC composite samples before removal from the AISI 4140 steel build plates. In addition, Fig. 2(b) shows the representation of a single tensile specimen, which was prepared in the form of a flat dog-bone specimen via wire Electrical Discharge Machining (EDM).

Following the removal from the build plate by wire EDM, samples of both the reinforced and unreinforced In718 materials were subjected to a standard heat treatment that is applied for wrought In718 in a tube furnace (OTF-1200X) [35]. Heat-treated samples (hereinafter indicated by HT) were held at 1050 °C in a furnace for 15 min, water cooled, held at 720 °C for 8 h, allowed to cool in the furnace, then held at 620 °C for 8 h and allowed to air cool.

2.3. Materials characterization

X-ray diffraction (XRD) was performed with an Aeris powder XRD instrument (Malvern Panalytical Ltd, Malvern, UK) at 35 kV and 40 mA with Cu-K_α ($\lambda = 1.5406$ Å) radiation at a 2θ range of 10–90° using a rate of 2°/min. Microstructures of the powders and LPBF samples were observed using a Zeiss Merlin high-resolution scanning electron microscope (SEM) (Carl Zeiss AG, Oberkochen, Germany), which is equipped with an energy dispersive spectrometer (EDX). Electron backscatter diffraction (EBSD) analyses were performed in the same SEM. An AccuPyc II 1340 gas pycnometer (Micromeritics) was used to measure the densities of the as-printed samples. The porosity fractions of as-printed samples were measured from SEM images by using ImageJ software (Java version) image processing. A Zeiss Vision 40 CrossBeam Focused Ion Beam (FIB) was utilized to prepare samples for scanning transmission electron microscopy (STEM). Following FIB, STEM was carried out in a JEOL 2010 TEM (JEOL Ltd., Tokyo, Japan) at 200 kV.

Vickers microhardness values of the LPBF samples were measured using a Struers/Emco-Test DuraScan Automatic Hardness Tester (Struers LLC, Cleveland, OH, USA) under a load of 0.5 kg (4.903 N) for 10 s. 10 indentations were performed on each sample and the final microhardness test results are expressed as the mean values of these 10 indentations along with the standard deviation. Tensile tests were performed at room temperature in an Instron 5969 with a strain rate of 2×10^{-4}/s and repeated three times for each sample category to verify results. The tensile displacement and the strain were precisely recorded by a non-contact AVE2 video extensometer.

3. Results and discussion

First, the morphology and microstructure of the In718–2 vol% SiC_{nw} powders were examined through SEM and EDX elemental mapping analysis after high-speed blending followed by ball milling (Fig. 3). Based on a comparison of Figs. 1(a) and 3(a), it is clear that the spherical shape of the In718 particles is maintained after powder processing, which is important to ensure good powder spreading during the LPBF process [40]. Moreover, EDX analysis shows overlapping Si and C signals well distributed across the particles, which supports that the In718 particle surfaces are uniformly decorated with SiC nanowires. Please note that the bright C region denoted by the red arrow in Fig. 3(f) indicates signal from bare carbon tape, where the particles do not exist.

Cross-sections of the ball-milled In718+SiC powders were further analyzed via TEM to understand the nanowire distribution on the In718 particles. Fig. 4 provides a TEM image and the corresponding EDX mapping results obtained from a cross-section of a single In718 particle following ball milling with the SiC_{nw}. We found that approximately 200–300 nm of SiC was continuously coated on the In718 particles, which may suggest the success of the preliminary blending process for declustering the nanowires and allowing their distribution. Following that process, a relatively low ball milling speed (600 rpm) and duration (30 min) provided sufficient mechanical energy for effective and continuous deposition of the declustered nanowires onto the In718 particles without severe plastic deformation induced shape changes.

XRD patterns were obtained from In718 and In718+SiC specimens after LPBF, with and without the post-printing heat treatment to understand the evolution of phases (Fig. 5(a)). Based on the XRD patterns, both In718 and In718+SiC composite samples display the typical face-centered cubic γ (Ni-Cr-Fe) matrix phase. Apart from this, both as-printed and HT'ed In718+SiC have minor amounts of (Nb,Ti)C phases, which were not detected in either case for the pristine In718 sample. The presence of the XRD peaks of (Nb,Ti)C phases could be seen in Fig. S1 of the Supplementary Materials. This suggests the presence of an exchange reaction between the In718 base alloy and the SiC during the melting/solidification process. It is believed that the Nb and Ti, which exist around 4.8 and 0.9 wt% in the In718 composition, respectively, reacted with C from dissolved SiC, resulting in the appearance of (Nb,Ti)C phases in the XRD patterns. We note that it is impossible to discriminate the γ′ and γ″ precipitates through basic XRD of heat-treated samples since they overlap with the XRD peaks of the γ phase [36]. Therefore, the presence of these precipitates in HT'ed In718+SiC was confirmed through TEM EDX mapping analysis, which is shown in Fig. 5 (b-k). The TEM image of Fig. 5(b) exhibits rod-like bright phase regions with lengths ~10 nm, which are highlighted by yellow arrows. According to the EDX mapping results, those phase regions show Ni, Nb, Ti and Al elements and lack Fe and Cr, which matches expectations for the presence of γ′ and γ″ precipitates at the related regions. Although the γ′ phase primarily consists of Al and Ti elements, it also contains Nb [41]. On the other hand, the γ″ phase has Nb and Ti as its major components, but it may also contain some amount of Al. Therefore, it is hard to distinguish γ′ and γ″ on the EDX mapping results shown in Fig. 5(b-k).

In order to investigate the microstructures of the printed samples, secondary electron SEM images were obtained from cross-sections of In718 and In718+SiC with and without heat treatment after LPBF (Fig. 6 (a-h)). Notably, the unreinforced In718 alloys have a higher density of spherical and irregularly shaped porosities and cracks (indicated by red arrows) compared to the In718+SiC composites. These results are in contrast to those achieved by Cooper et al. [42], who dismissed SiC reinforcement of In625 in favor of TiC reinforcement due to excessive cracking during printing. The improved print quality achieved here is attributed in part to the dissolvability and heat dissipation effects of the SiC particles, in addition to the improved precision of the LPBF technology used in this study compared to that by Cooper et al., (e.g., 100 μm laser spot size here vs 850 μm spot size there). In other words, when the thermal conductivity of the ceramic nanoparticles is higher than that of Inconel 718 particles (10 W/(m·°C) at RT), it is possible to activate more effective heat dissipation in the liquid metal [43,44]. For instance, Gu et al. [44] demonstrated that TiC nanoparticles (23 W/(m·°C) at RT accelerate heat dissipation from the Inconel 718 molten pool during the LPBF process. It is possible that the SiC_{nw} used here with the In718 powders resulted in more effective heat dissipation during solidification, which increased the thermal gradient and cooling rate in the melt-pool and suppressed the defect formation resulting from

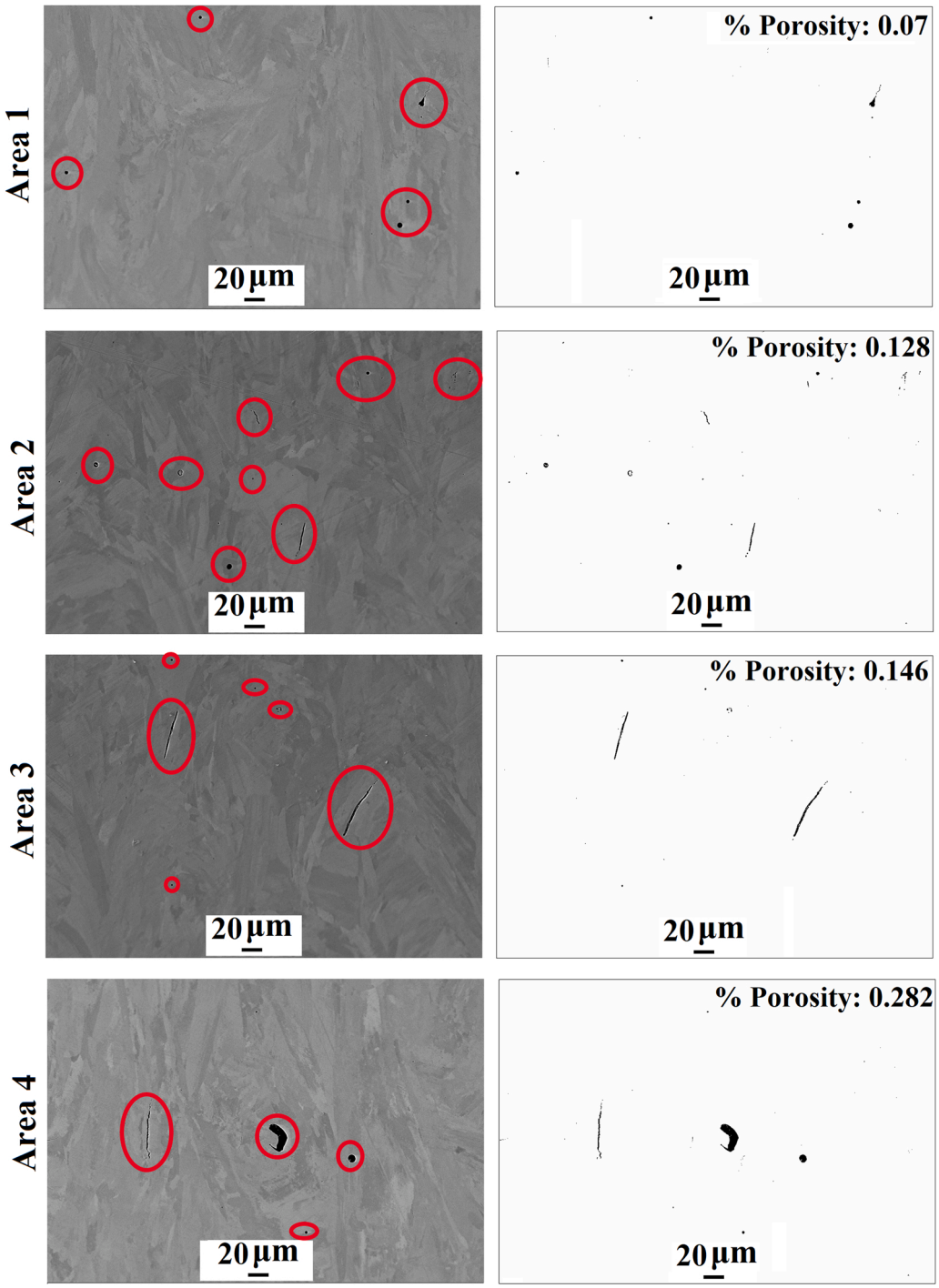

Fig. 7. Secondary electron SEM images obtained from as-printed In718 to calculate porosity fractions. The samples are cut along the build direction.

excessive laser energy input [45]. As such, excessive recoil pressure was suppressed and the formation of keyhole porosities and gas porosities was largely prevented [46]. Finally, cross-section images shown in Fig. S2 and Table S1 confirm that the melt pool sizes decrease with the incorporation of SiC into In718. The average melt pool width and depth of the as-printed In718 are 245.1 and 190.0 μm, respectively, whereas the average melt pool width and depth of In718+SiC are 189.1 and 146.9 μm, respectively. Nevertheless, further investigation is required to understand the effect of SiC incorporation into In718 on laser absorptivity during LPBF.

Additionally, EDX analysis results obtained from the points indexed as 1, 2, 3 and 4 show a higher concentration of Nb and Mo compared to the general EDX results obtained from the as-printed In718+SiC sample. This indicates the presence of Laves phases (indexed as yellow arrows). The XRD peaks of the Laves phases were not identified, possibly due to their relatively low volume fraction in the material system. The results of this analysis are provided in Table 3. It is apparent that the Laves phase precipitates, which form a chain-like distribution before HT, become more homogeneously distributed in the matrix (γ phase) after HT. Based on the EDX analysis performed at point 5, the related location in the HT'ed In718+SiC shows signals of carbon, Nb and Ti. These possibly indicate carbides of Nb and Ti and are notated by white arrows.

The average porosity in the as-printed In718 was calculated from 4 different cross-sectional secondary electron SEM images by using

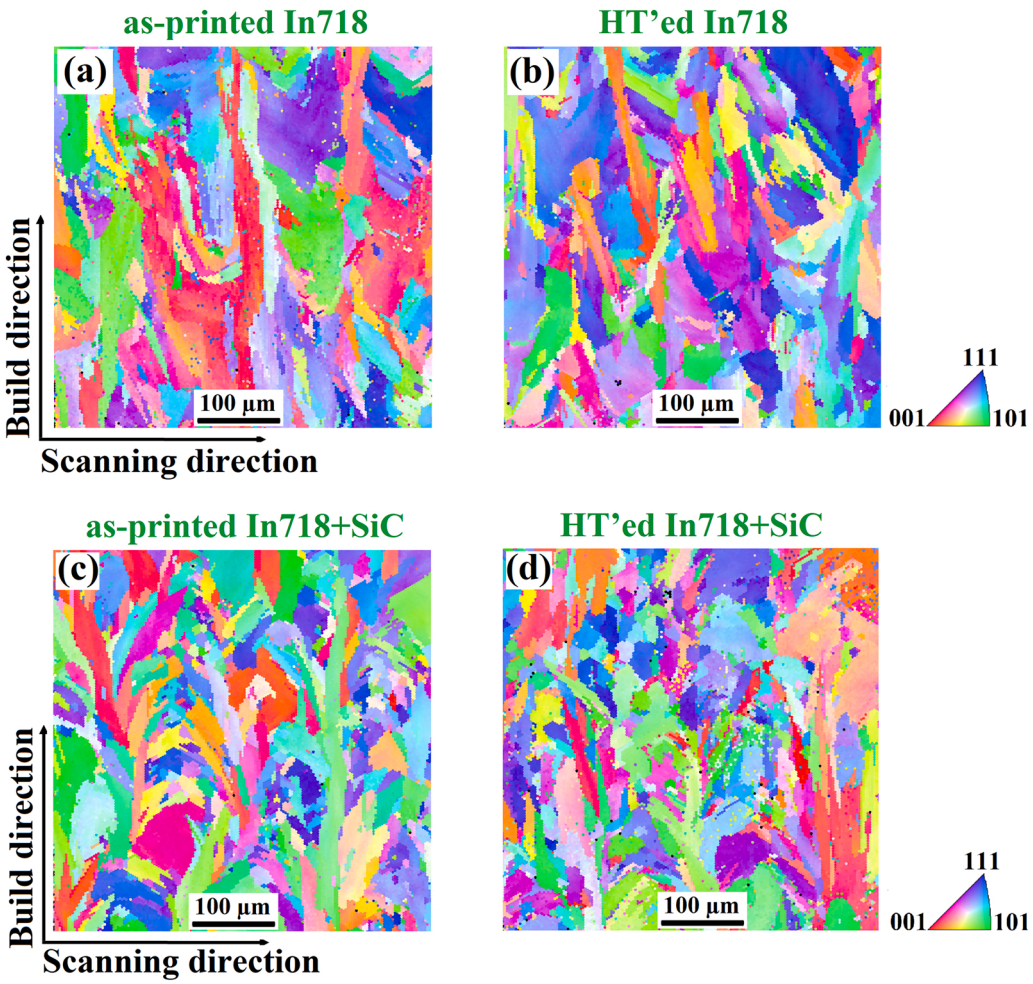

Fig. 8. EBSD analysis obtained from: (a) as-printed In718 (b) HT'ed In718, (c) as-printed In718+SiC and (d) HT'ed In718+SiC. The samples are cut along the build direction.

ImageJ software (Fig. 7). Please note that each picture corresponds to an area of 0.125 mm^2. Thus, the fraction of porosity calculation was made on a 0.5 mm^2 area in total. Results calculated from binary images show that an average of 0.1% porosity is present in the as-printed In718. As mentioned above, the related defects were not seen in In718+SiC composites. Additionally, the densities of as-printed In718 and as-printed In718+SiC are 8.19 ± 0.004 g/cm^3 and 8.12 ± 0.002 g/cm^3, and the relative densities are calculated to be 99.6% and 99.9%, respectively, by assuming the theoretical densities of In718 and SiC are 8.22 g/cm^3 [47,48] and 3.21 g/cm^3 [49,50]. It is important to note that the density of the LPBF In718 could be further increased by fine-tuning the parameter set. However, the 99.6% relative density value for as-printed In718 is consistent with the literature, which used the same original EOS parameter set to produce In718[51]. The point we want to make is that the SiC incorporation does increase the relative density and significantly reduce the porosity of LPBF In718 under same LPBF printing conditions.

EBSD analysis was performed on as-printed In718, HT'ed In718, as-printed In718+SiC and HT'ed In718+SiC samples to extract the grain size, shape and orientation maps (Fig. 8(a-d)). We observe long columnar grains in the as-printed In718 and In718+SiC samples (Fig. 8 (a, c)). However, the grains appear slightly smaller in the composite material compared to the unreinforced alloy. It could be assumed that the incorporation of SiC contributed to the refinement of grain size during LPBF. On the other hand, the grain structure becomes less columnar in both samples after HT, as shown in Fig. 8(b, d), due to the recrystallization phenomena taking place through the grains during HT.

Fig. 9 presents the misorientation angle and grain area fractions of In718 and In718+SiC in the as-printed and HT'ed states. As displayed in Fig. 9(a), low-angle boundaries (0–5°) are the major features in the as-printed In718. This is expected as thermal stresses during LPBF cause high dislocation density regions and facilitate the formation of low-angle grain boundaries [52,53]. Comparatively, the misorientation angle distribution pattern is different in the as-printed composite. As shown in Fig. 9(e) the incorporation of SiC into In718 significantly increases the fraction of high-angle grain boundaries. Furthermore, grain size distributions of the as-printed unreinforced alloy and reinforced composite were also slightly different. Since the aspect ratio of the grains was high, we measured the length (size along the build direction) and width (size perpendicular to the build direction) of the grains using ImageJ software. The average grain lengths or grain sizes along the build direction of the as-printed In718, HT'ed In718, as-printed In718+SiC and HT'ed In718+SiC are 105.2, 97.6, 91.6 and 70.2 µm, respectively. Gathered data of the misorientation angle and grain size values from EBSD analysis can be found in Tables S2 and S3 in Supplementary Materials. Based on these results, it can be stated that the addition of SiC also had a slightly positive effect on grain refinement during solidification.

STEM imaging and corresponding EDX mapping analysis were carried out to interpret the microstructures of the as-printed and HT'ed In718+SiC (Fig. 10). As observed in Fig. 10 (a), there are spherical particles ~50 nm in diameter in the microstructure of as-printed In718+SiC, which are marked with the letter "A" and yellow arrows. EDX data from these regions indicates Al and O signals, as seen in Fig. 10

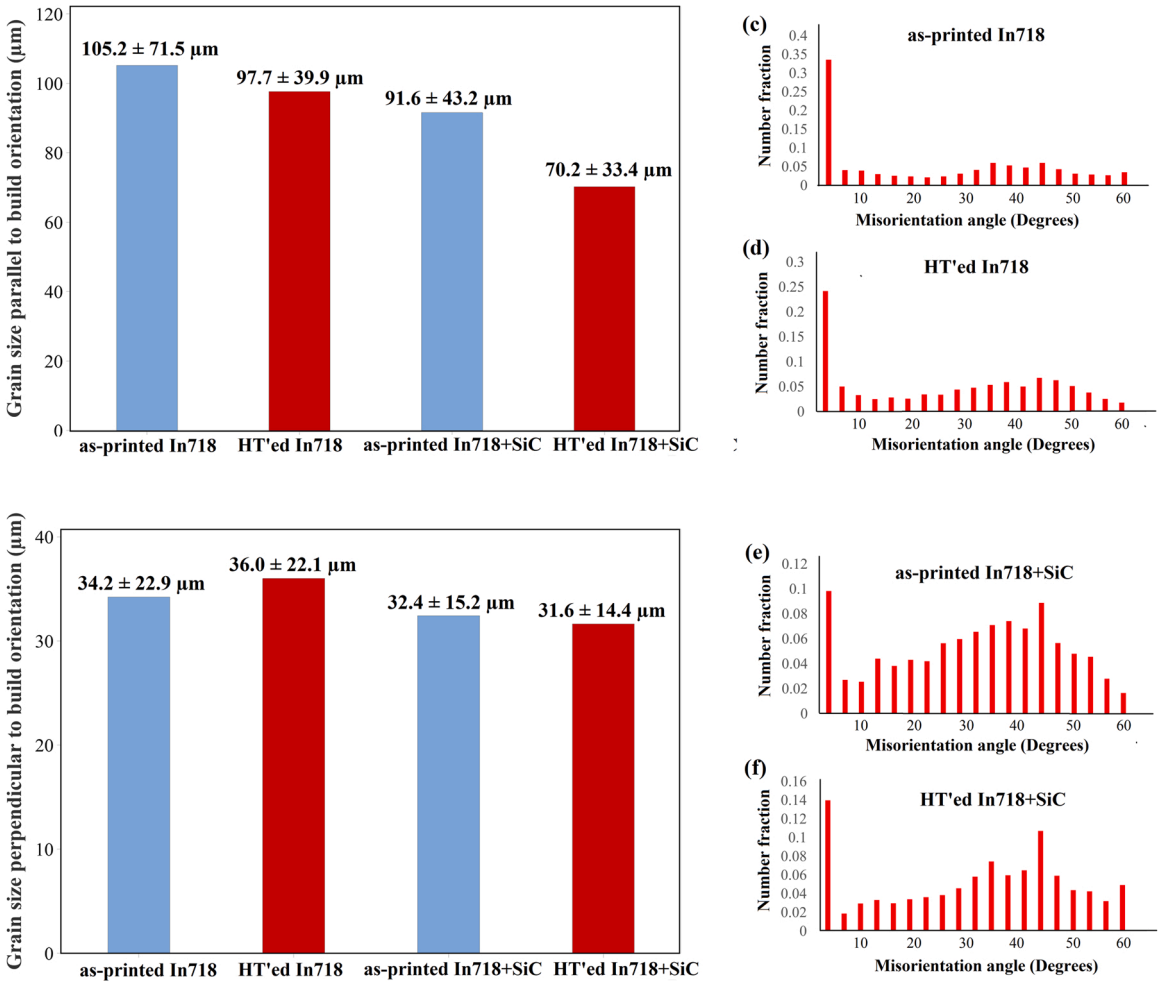

Fig. 9. Grain size distribution and misorientation angle distribution plots of: In718 and In718+SiC in the as-printed and heat-treated conditions.

(e and i). These are most likely nanoparticulate Al_2O_3 inclusions, which likely formed during the LPBF process due to the interaction of the Al species in In718 with trace oxygen in the build chamber [54]. Their corresponding EDX results are also shown in Fig. S3 and Table S4 in Supplementary Materials. Moreover, there were also strong overlapping signals of Nb, Ti and C surrounding the Al_2O_3 precipitates and exhibiting a spiral morphology, which are predicted to be metal carbides; these are marked as "C" and indicated with white arrows in Fig. 10 (g, h and j). Another phase region observed was indexed as "S" with red arrows and shown in Fig. 10 (a). This region shows strong signals of Nb, Ti and Si, as observed in Fig. 10 (f-h), and is most likely a (Nb, Ti)-based silicide. It is well known that Nb and Ti tend to form silicides in the presence of free Si particles in superalloy microstructures [55]. Thus, it is understood that the decomposition of the SiC enabled (Nb,Ti)-based silicide formation during LPBF. Fig. 10 (l) shows a spherical Al_2O_3 particle surrounded with dark phases that exhibit strong Nb, Ti, Mo and C signals in the EDX mapping analysis shown in Fig. 10 (g, h and j). This confirms that the related metal carbides (MCs) nucleate around Al_2O_3 particles during LPBF.

We believe that the decomposition of the SiC during LPBF not only boosted (Nb,Ti)-based silicide formation but also (Nb,Ti)-based carbide formation. Furthermore, the rapid temperature changes associated with the laser melting process appear to have resulted in the dissolution of the SiC nanowires, resulting in the in-situ formation of (Nb,Ti)-based silicides and carbides. In other words, Si and C acted as silicide and carbide sources as a result of the in-situ partial decomposition of the SiC_{nw} in the microstructure and further strengthened the matrix as secondary phases, which will be discussed later. It is reported in the literature that increasing C content in In718 alloys promotes a higher fraction of MCs during casting or LPBF, which eliminates hot cracking propagation during solidification [56,57]. Therefore, it is important to recall Fig. 6 (b), where as-printed In718+SiC exhibited a defect-reduced microstructure contrary to the unreinforced In718. These results align well with the discussed literature and suggest that free C-particles coming from SiC_{nw} dissolution tailored a near defect-free microstructure during LPBF of In718+SiC. It is also important to note that the morphologies of the (Nb,Ti)-based carbides evolved from spiral and rod-type morphologies to cornered particle (100–200 nm) morphologies after HT.

Fig. 10 (m-w) shows the STEM image and corresponding EDX mapping analysis of HT'ed In718+SiC. It is clear that the spherical Al_2O_3 phase regions (indexed as yellow arrows), which had formed during LPBF, also remained after heat treatment. It is also notable that (Nb, Ti)-based carbide phases (indexed as white arrows) have a particle-like morphology (60–200 nm size) with an average size of around 90 nm compared to the spiral morphology of those observed in as-printed In718+SiC.

Next, micro-hardness testing was performed to evaluate the local mechanical properties of each printed sample. Table 4 shows the average microhardness results obtained from as-printed In718, HT'ed In718, as-printed In718+SiC, and HT'ed In718+SiC, respectively. Both the unreinforced In718 and the In718+SiC show higher hardness after HT. As shown in Fig. 6(c, d, g and h) above, fine precipitates become homogeneously distributed after HT in both samples. That is assumed to be the most important factor in the augmented hardness after HT. The

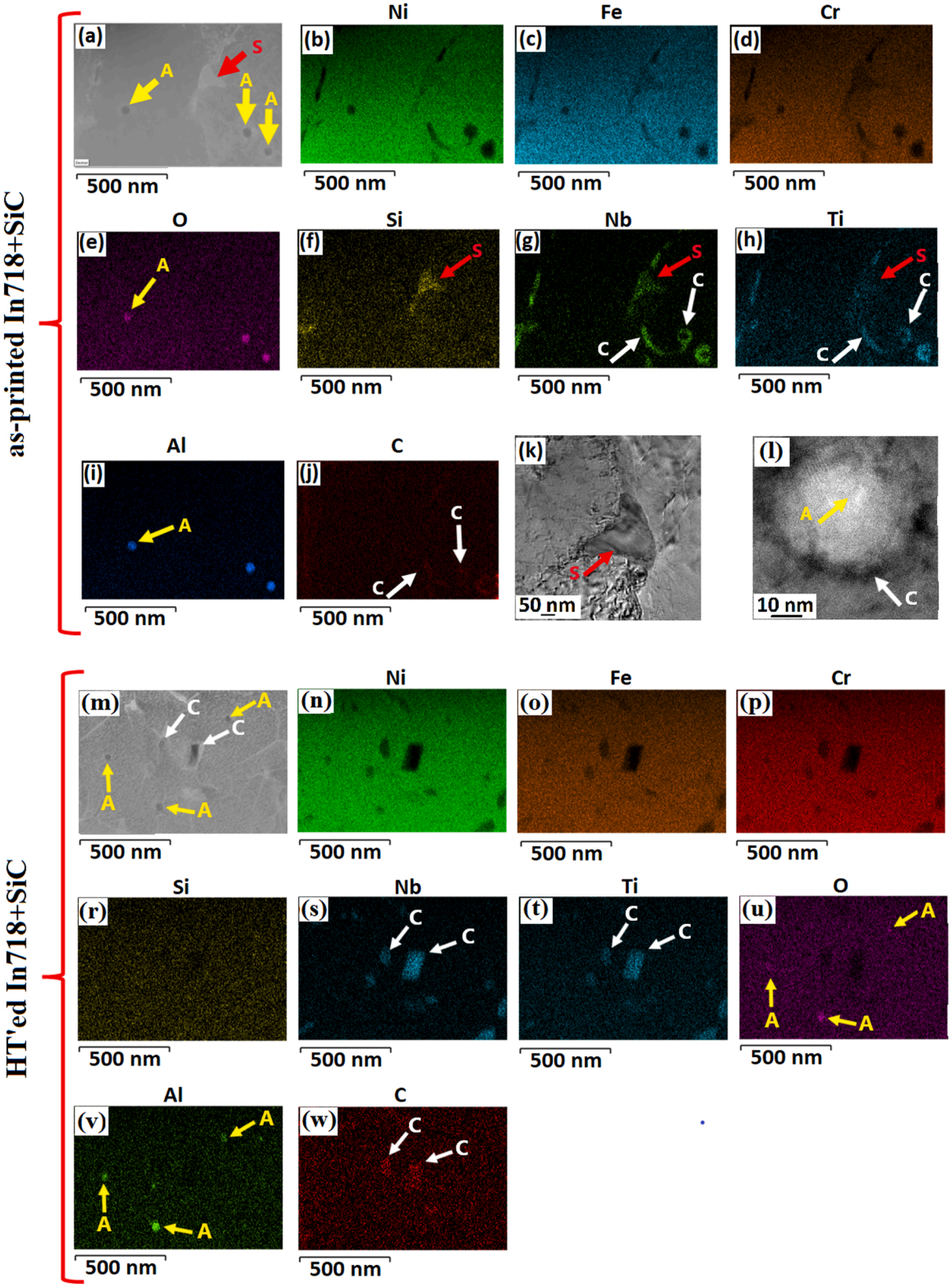

Fig. 10. STEM images and corresponding EDX mapping analyses obtained from: (a-l) as-printed In718+SiC and (m-w) HT'ed In718+SiC.

microhardness of the as-printed In718+SiC was measured to be 14% higher than the as-printed In718. It is believed that the decomposition of SiC favored fine (Nb, Ti)-based silicide and (Nb, Ti)-based carbide formation particles and this led to the increase in hardness values in the In718+SiC nanocomposite.

Lastly, tensile testing was performed on bulk samples cut from blocks fabricated by LPBF, as described in the methods section. Fig. 11 shows the room temperature tensile stress-strain curves obtained from the additively manufactured In718 and In718+SiC with and without heat treatment. In addition, comparison of yield strength (σ_y), ultimate tensile strength (σ_{UTS}) and elongation values of the as-printed and HT'ed samples produced in this study are compared with those of other studies in the literature; these are listed in Table 5. σ_y and σ_{UTS} of the unreinforced In718 alloy and In718+SiC increase remarkably after heat

Table 4
Average microhardness of as-printed In718, HT'ed In718, as-printed In718+SiC, and HT'ed In718+SiC samples.

Material	Microhardness value (HV)
In718 as-printed	319.1 ± 7.9
In718 HT'ed	436.3 ± 11.3
In718+SiC as-printed	363 ± 10.2
In718+SiC HT'ed	468.9 ± 8.7

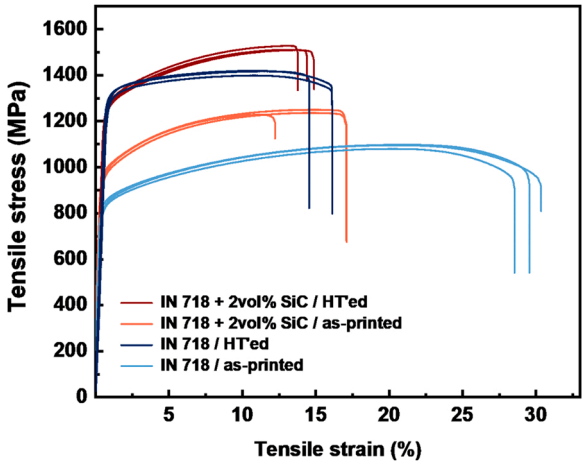

Fig. 11. Room temperature tensile stress-strain curves of as-printed and HT'ed In718 and In718+SiC.

Table 5
Room temperature tensile results obtained from LPBF In718 and LPBF In718+SiC with and without heat treatment.

Sample no	Material	YS (MPa)	UTS (MPa)	Elongation (%)
1	In718 as-printed (this study)	826	1095	30.3
2	In718 HT'ed (this study)	1264	1398	16.1
3	In718+SiC as-printed (this study)	963	1250	17.1
4	In718+SiC HT'ed (this study)	1251	1527	13.8
5	In718 + 2 wt% TiC as-printed[32]	774	1029	12.3
6	In718 + 2 wt% TiC HT'ed[32]	1144	1380	9.1
7	In718 + 1 wt% Y_2O_3 as-printed[62]	850	1100	17
8	AMS 5662 G specification for wrought In718[35]	1035–1167	1275–1400	12–21

treatment, which agrees with the hardness test results. This result is expected, as the strengthening benefits of heat treatment in In718 are well documented [58,59]. Notably though, σ_y and σ_{UTS} of the as-printed In718+SiC were 16% and 12% higher, respectively, than those of the unreinforced alloy. HT'ed In718+SiC composite has almost the same σ_y as the HT'ed In718. However, σ_{UTS} of the In718+SiC composite is 1527 MPa, which is 10% higher than that of the HT'ed unreinforced alloy. These results prove the beneficial effects of the silicide/carbide formation on the alloy.

Prior to the heat treatment, the in-situ produced silicide and carbide precipitates resulting from the SiC composite addition evidently act as a primary barrier to dislocation movement, thereby resulting in the increase in both σ_y and σ_{UTS} observed. Following the heat treatment, it is known that the newly formed uniform distributions of γ' and γ'' precipitates harden against plastic deformation in unreinforced In718, and the near equal yield strengths observed suggest that the stress required to induce dislocation motion against these phases remains the dominant barrier regardless of reinforcement. Yet it is evident from the plot that the HT'ed composite shows a higher strain hardening rate compared to the HT'ed unreinforced alloy. This can be attributed to the additional silicide and carbide precipitates that have been relegated to the narrow γ bands. It may be understood that these additional precipitates serve a dual purpose, inducing a pinning effect that both suppresses γ-grain coarsening during heat treatment and restricts dislocation movement after heat treatment, which is in good agreement with current literature on the effects of carbides in In718 [60,61]. The result is that, despite similar yield strengths, SiC reinforcement produces a significant effect on the strain hardening and ultimate tensile strength. Moreover, the elongations of the composite and the unreinforced alloy are comparable. This is a positive result, as the total elongation of the unreinforced alloy decreases to nearly half after HT, but the total elongation of the composite changes very little with HT, by only about 3%. To summarize highlights of the tensile results, the In718+SiC composite shows industrially acceptable elongation after both LPBF and HT, ranging around 12–17%. It is important to note that the HT'ed composite shows a higher σ_y and σ_{UTS}. Moreover, compared to the other In718-based composites produced via LPBF, the composite in this study shows especially a greater σ_{UTS} than those of reinforced with TiC or Y_2O_3 [32,62]. We conclude that the incorporation of the SiC into the In718 during LPBF contributes to the increased tensile strength of the In718 alloys while maintaining good tensile elongation, which is an important requirement for engineering metallic alloys. SiC nanowires are considered to indirectly contribute to the mechanical properties of In718 through the formation of (Nb,Ti)-based carbides and (Nb,Ti)-based silicides.

Fig. 12 shows the SEM images taken from the fractured surfaces of as-printed In718, as-printed In718+SiC, HT'ed In718, and HT'ed In718+SiC, respectively. The fracture surface of the as-printed unreinforced In718 alloy is covered with dimples, such as the features indicated by the red square in Fig. 12 (a). The dimples indicate intensive plastic deformation. The fracture surface of the heat-treated In718 shows regions of flat topography in addition to the dimples, which indicates that the fracture mechanism was not purely ductile but also partially brittle (Fig. 12 (b)). This is within expectations since the total tensile elongation of the unreinforced alloy decreases from 30.3% to 16.1% after HT. For the In718+SiC composites, both as-printed and HT'ed samples show a mixture of dimples and sharp textures as well (Fig. 12 (c, d)).

4. Conclusion

We additively manufactured a new In718-based metal matrix composite material reinforced by SiC nanowires. Based on cross-sectional analyses of the specimens prepared by LPBF, the dissolution of the SiC nanowires resulted in the in-situ formation of (Nb,Ti)-based silicides and carbides. Although the nanowire geometry was initially considered desirable for the expected strengthening contribution of its large surface area after printing, it is theorized that the nanowire dissolution process compounded with the grain-pinning effects of the newly formed nanoparticles and positively contributed to grain geometry and the prevention of defects. The as-printed microstructure of the reinforced In718 was also found to be flaw-reduced and to have a smaller average grain size compared to unreinforced In718, indicating the viability of this manufacturing method compared to previous attempts at nickel-based SiC MMCs, which have suffered from significant cracking and poor print quality.

Based on hardness and tensile testing data, we conclude that in-situ formed silicides and carbides during printing and their associated microstructural changes had notable strengthening effects on the In718 materials. The as-printed In718 reinforced by SiC was found to have a 16% increase in σ_y and a 12% increase in σ_{UTS} compared to the

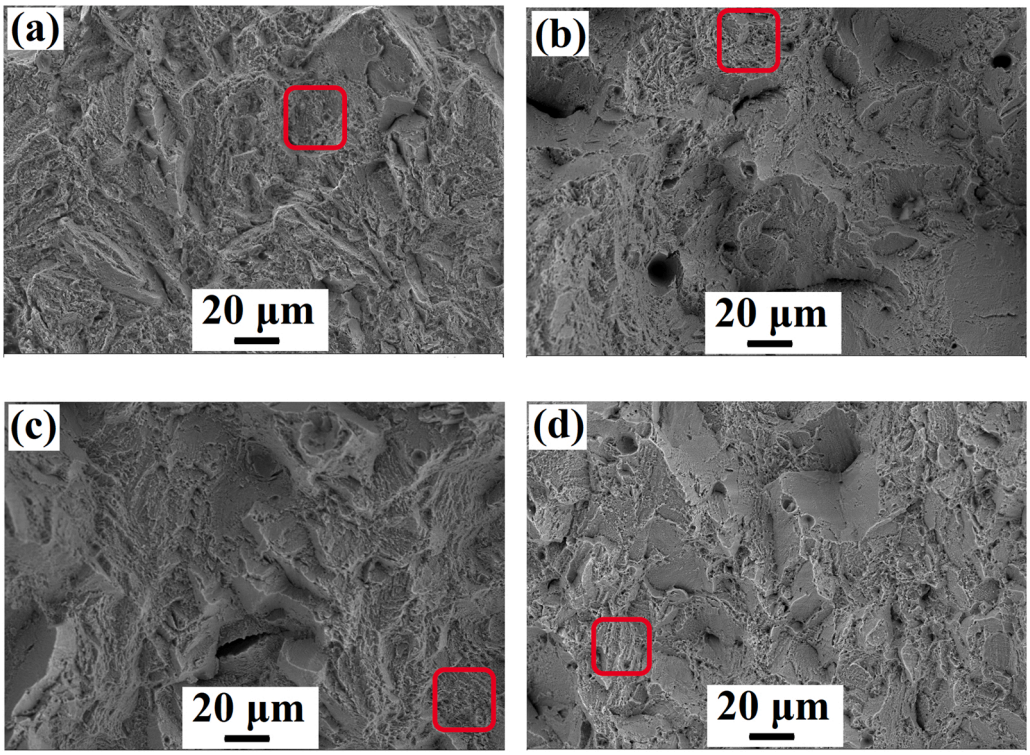

Fig. 12. SEM images taken from fracture surfaces of: (a) as-printed In718 (b) as-printed In718+SiC, (c) HT'ed In718 and (d) HT'ed In718+SiC.

unreinforced material. Following the application of a standard heat treatment procedure to the printed specimens, σ_y of the reinforced and unreinforced specimens were found to be nearly identical. Moreover, those samples reinforced by SiC were found to have a remarkable increase in strain hardening, resulting in a σ_{UTS} increase of 10% for the MMC materials, along with a maintenance of uniform ductility for preservation of ~14% total tensile elongation. These results indicate great promise in this reinforcement approach as a versatile and scalable method for increasing the load capabilities and overall lifetime of In718 materials in extreme environments such as nuclear reactors or high-temperature gas turbines. They also suggest the value of in-situ reaction for forming reinforcing particles during laser additive manufacturing in general, and we believe there will be great merit in expanding the method to more direct microalloying of Si and C as well as to new composite combinations in the near future.

CRediT authorship contribution statement

Emre Tekoğlu: Writing – review & editing, Writing – original draft, Investigation, Data curation. **Alexander D. O'Brien:** Writing – review & editing, Writing – original draft, Investigation, Data curation. **Jian Liu:** Writing – review & editing, Writing – original draft, Investigation, Data curation. **Baoming Wang:** Data curation. **Sina Kavak:** Data curation. **Yong Zhang:** Data curation. **So Yeon Kim:** Data curation. **Shitong Wang:** Data curation. **Duygu Ağaoğulları:** Data curation. **Wen Chen:** Writing – review & editing, Visualization, Validation, Supervision, Conceptualization. **A. John Hart:** Writing – review & editing, Writing – original draft, Validation, Supervision. **Ju Li:** Writing – review & editing, Writing – original draft, Visualization, Validation, Supervision, Resources, Funding acquisition, Conceptualization.

Declaration of Competing Interest

The authors declare that they have no known competing financial interests or personal relationships that could have appeared to influence the work reported in this paper.

Data Availability

Data will be made available on request.

Acknowledgements

This work was supported by Eni S.p.A. through the MIT Energy Initiative, The Scientific and Technological Research Council of Turkey (TUBITAK) under Grant No. 1059B192000941, and ARPA-E (DE-AR0001434). WC acknowledges support by the National Science Foundation (DMR-2004429). ADO acknowledges support by NSF GRFP Award #4999143677. SK and DA acknowledge the support by Istanbul Technical University Scientific Research Projects Unit with a project (No: MUA-2021–43196) entitled "Production and Characterization of Boron Containing Metallic Nanocomposites via Additive Manufacturing".

Appendix A. Supporting information

Supplementary data associated with this article can be found in the online version at doi:10.1016/j.addma.2023.103478.

References

[1] L. Yang, C. O'Neil, Y. Wu, The use of electropolishing surface treatment on IN718 parts fabricated by laser powder bed fusion process. Solid Freeform Fabrication 2017: Proceedings of the 28th Annual International Solid Freeform Fabrication Symposium - An Additive Manufacturing Conference, SFF 2017,, 2020, pp. 2493–2502.

[2] N. Raghavan, R. Dehoff, S. Pannala, S. Simunovic, M. Kirka, J. Turner, N. Carlson, S.S. Babu, Numerical modeling of heat-transfer and the influence of process parameters on tailoring the grain morphology of IN718 in electron beam additive manufacturing, Acta Mater. (2016), https://doi.org/10.1016/j.actamat.2016.03.063.

[3] X. Wang, X. Gong, K. Chou, Review on powder-bed laser additive manufacturing of Inconel 718 parts, Proc. Inst. Mech. Eng. B J. Eng. Manuf. (2017), https://doi.org/10.1177/0954405415619883.

[4] E. Hosseini, V.A. Popovich, A review of mechanical properties of additively manufactured Inconel 718, Addit. Manuf. 30 (2019), 100877, https://doi.org/10.1016/j.addma.2019.100877.

[5] B. Zhang, G. Bi, P. Wang, J. Bai, Y. Chew, M.S. Nai, Microstructure and mechanical properties of Inconel 625/nano-TiB2 composite fabricated by LAAM, Mater. Des. (2016), https://doi.org/10.1016/j.matdes.2016.08.078.

[6] B. Zhang, G. Bi, S. Nai, C.N. Sun, J. Wei, Microhardness and microstructure evolution of TiB2 reinforced Inconel 625/TiB2 composite produced by selective laser melting, Opt. Laser Technol. (2016), https://doi.org/10.1016/j.optlastec.2016.01.010.

[7] M.Y. Shen, X.J. Tian, D. Liu, H.B. Tang, X. Cheng, Microstructure and fracture behavior of TiC particles reinforced Inconel 625 composites prepared by laser additive manufacturing, J. Alloy. Compd. (2018), https://doi.org/10.1016/j.jallcom.2017.10.280.

[8] S.H. Kim, G.H. Shin, B.K. Kim, K.T. Kim, D.Y. Yang, C. Aranas, J.P. Choi, J.H. Yu, Thermo-mechanical improvement of Inconel 718 using ex situ boron nitride-reinforced composites processed by laser powder bed fusion, Sci. Rep. (2017), https://doi.org/10.1038/s41598-017-14713-1.

[9] J. Shi, Y. Wang, Development of metal matrix composites by laser-assisted additive manufacturing technologies: a review, J. Mater. Sci. (2020), https://doi.org/10.1007/s10853-020-04730-3.

[10] M.P. Behera, T. Dougherty, S. Singamneni, Conventional and additive manufacturing with metal matrix composites: a perspective, Procedia Manuf. 30 (2019) 159–166, https://doi.org/10.1016/J.PROMFG.2019.02.023.

[11] J. Rui-song, W. Wen-hu, S. Guo-dong, W. Zeng-qiang, Experimental investigation on machinability of in situ formed TiB2 particles reinforced Al MMCs, J. Manuf. Process 23 (2016) 249–257, https://doi.org/10.1016/j.jmapro.2016.05.004.

[12] M. Karbalaei Akbari, H.R. Baharvandi, O. Mirzaee, Fabrication of nano-sized Al2O3 reinforced casting aluminum composite focusing on preparation process of reinforcement powders and evaluation of its properties, Compos B Eng. 55 (2013) 426–432, https://doi.org/10.1016/j.compositesb.2013.07.008.

[13] Q. Hu, H. Zhao, F. Li, Microstructures and properties of SiC particles reinforced aluminum-matrix composites fabricated by vacuum-assisted high pressure die casting, Mater. Sci. Eng. A. 680 (2017) 270–277, https://doi.org/10.1016/j.msea.2016.10.090.

[14] B. Zhang, Principles, methods, formation mechanisms, and structures of nanomaterials prepared via solid-phase syntheses, Phys. Fundam. Nanomater. (2018), https://doi.org/10.1016/b978-0-12-410417-4.00004-6.

[15] H. Brooks, K. Brigden, Design of conformal cooling layers with self-supporting lattices for additively manufactured tooling, Addit. Manuf. (2016), https://doi.org/10.1016/j.addma.2016.03.004.

[16] M. Mazur, M. Leary, M. McMillan, J. Elambasseril, M. Brandt, SLM additive manufacture of H13 tool steel with conformal cooling and structural lattices, Rapid Prototyp. J. (2016), https://doi.org/10.1108/RPJ-06-2014-0075.

[17] A. Hussein, L. Hao, C. Yan, R. Everson, P. Young, Advanced lattice support structures for metal additive manufacturing, J. Mater. Process Technol. (2013), https://doi.org/10.1016/j.jmatprotec.2013.01.020.

[18] R. Wauthle, B. Vrancken, B. Beynaerts, K. Jorissen, J. Schrooten, J.P. Kruth, J. van Humbeeck, Effects of build orientation and heat treatment on the microstructure and mechanical properties of selective laser melted Ti6Al4V lattice structures, Addit. Manuf. (2015), https://doi.org/10.1016/j.addma.2014.12.008.

[19] S. Liu, Y.C. Shin, Additive manufacturing of Ti6Al4V alloy: A review, Mater. Des. (2019), https://doi.org/10.1016/j.matdes.2018.107552.

[20] D. Herzog, V. Seyda, E. Wycisk, C. Emmelmann, Additive manufacturing of metals, Acta Mater. (2016), https://doi.org/10.1016/j.actamat.2016.07.019.

[21] J. Dawes, R. Bowerman, R. Trepleton, Introduction to the additive manufacturing powder metallurgy supply chain, Johns. Matthey Technol. Rev. (2015), https://doi.org/10.1595/205651315X688686.

[22] C. Sun, Y. Wang, M.D. McMurtrey, N.D. Jerred, F. Liou, J. Li, Additive manufacturing for energy: A review, Appl. Energy 282 (2021), https://doi.org/10.1016/j.apenergy.2020.116041.

[23] A. Gisario, M. Kazarian, F. Martina, M. Mehrpouya, Metal additive manufacturing in the commercial aviation industry: A review, J. Manuf. Syst. (2019), https://doi.org/10.1016/j.jmsy.2019.08.005.

[24] M. Kniepkamp, J. Fischer, E. Abele, Dimensional accuracy of small parts manufactured by micro selective laser melting. Solid Freeform Fabrication 2016: Proceedings of the 27th Annual International Solid Freeform Fabrication Symposium - An Additive Manufacturing Conference, SFF 2016,, 2016.

[25] S.L. Sing, F.E. Wiria, W.Y. Yeong, Selective laser melting of lattice structures: A statistical approach to manufacturability and mechanical behavior, Robot Comput. Integr. Manuf. (2018), https://doi.org/10.1016/j.rcim.2017.06.006.

[26] U. Yildirim, S. Abanteriba, Manufacture, qualification and approval of new aviation turbine fuels and additives, Procedia Eng. (2012), https://doi.org/10.1016/j.proeng.2012.10.142.

[27] J.C. Najmon, S. Raeisi, A. Tovar, Review of additive manufacturing technologies and applications in the aerospace industry, Addit. Manuf. Aerosp. Ind. (2019), https://doi.org/10.1016/b978-0-12-814062-8.00002-9.

[28] J. Shi, Y. Wang, Development of metal matrix composites by laser-assisted additive manufacturing technologies: a review, (n.d.). https://doi.org/10.1007/s10853-020-04730-3.

[29] Z. Zhang, Q. Han, S. Yang, Y. Yin, J. Gao, R. Setchi, Laser powder bed fusion of advanced submicrometer TiB2 reinforced high-performance Ni-based composite, Mater. Sci. Eng.: A 817 (2021), 141416, https://doi.org/10.1016/j.msea.2021.141416.

[30] V. Mandal, P. Tripathi, A. Kumar, S.S. Singh, J. Ramkumar, A study on selective laser melting (SLM) of TiC and B4C reinforced IN718 metal matrix composites (MMCs, J. Alloy. Compd. 901 (2022), 163527, https://doi.org/10.1016/J.JALLCOM.2021.163527.

[31] D. Gu, H. Zhang, D. Dai, M. Xia, C. Hong, R. Poprawe, Laser additive manufacturing of nano-TiC reinforced Ni-based nanocomposites with tailored microstructure and performance, Compos B Eng. 163 (2019) 585–597, https://doi.org/10.1016/j.compositesb.2018.12.146.

[32] X. Yao, S.K. Moon, B.Y. Lee, G. Bi, Effects of heat treatment on microstructures and tensile properties of IN718/TiC nanocomposite fabricated by selective laser melting, Int. J. Precis. Eng. Manuf. 18 (2017) 1693–1701, https://doi.org/10.1007/s12541-017-0197-y.

[33] M. Yamamoto, Y. Nishimura, M. Hayashida, Influence of Al particles as infiltration promoters on the interfacial reaction and mechanical property of a continuous SiC fiber/AZ91 composite fabricated by a low-pressure infiltration method, J. Alloy. Compd. 887 (2021), 161461, https://doi.org/10.1016/j.jallcom.2021.161461.

[34] C. Qiu, Y. Su, B. Chen, J. Yang, Z. Li, Q. Ouyang, Q. Guo, D. Xiong, D. Zhang, First-principles investigation of interfacial stability, mechanical behavior and failure mechanism of β-SiC(1 1 1)/Al(1 1 1) interfaces, Comput. Mater. Sci. 175 (2020), 109608, https://doi.org/10.1016/j.commatsci.2020.109608.

[35] G.A. Rao, M. Kumar, M. Srinivas, D.S. Sarma, Effect of standard heat treatment on the microstructure and mechanical properties of hot isostatically pressed superalloy inconel 718, Mater. Sci. Eng.: A 355 (2003) 114–125, https://doi.org/10.1016/S0921-5093(03)00079-0.

[36] Y. Gao, D. Zhang, M. Cao, R. Chen, Z. Feng, R. Poprawe, J.H. Schleifenbaum, S. Ziegler, Effect of δ phase on high temperature mechanical performances of Inconel 718 fabricated with SLM process, Mater. Sci. Eng.: A 767 (2019), 138327, https://doi.org/10.1016/J.MSEA.2019.138327.

[37] S. Sui, H. Tan, J. Chen, C. Zhong, Z. Li, W. Fan, A. Gasser, W. Huang, The influence of Laves phases on the room temperature tensile properties of Inconel 718 fabricated by powder feeding laser additive manufacturing, Acta Mater. 164 (2019) 413–427, https://doi.org/10.1016/J.ACTAMAT.2018.10.032.

[38] C. Kantzos, J. Pauza, R. Cunningham, S.P. Narra, J. Beuth, A. Rollett, An Investigation of Process Parameter Modifications on Additively Manufactured Inconel 718 Parts, J Mater Eng Perform. 28 (n.d.). https://doi.org/10.1007/s11665–018-3612–3.

[39] D. Zhang, W. Niu, X. Cao, Z. Liu, Effect of standard heat treatment on the microstructure and mechanical properties of selective laser melting manufactured Inconel 718 superalloy, Mater. Sci. Eng.: A 644 (2015) 32–40, https://doi.org/10.1016/J.MSEA.2015.06.021.

[40] D. Yao, X. Liu, J. Wang, W. Fan, M. Li, H. Fu, H. Zhang, X. Yang, Q. Zou, X. An, Numerical insights on the spreading of practical 316 L stainless steel powder in SLM additive manufacturing, Powder Technol. 390 (2021) 197–208, https://doi.org/10.1016/J.POWTEC.2021.05.082.

[41] K. Kulawik, P.A. Buffat, A. Kruk, A.M. Wusatowska-Sarnek, A. Czyrska-Filemonowicz, Imaging and characterization of γ′ and γ″ nanoparticles in Inconel 718 by EDX elemental mapping and FIB–SEM tomography, Mater. Charact. 100 (2015) 74–80, https://doi.org/10.1016/J.MATCHAR.2014.12.012.

[42] D.E. Cooper, N. Blundell, S. Maggs, G.J. Gibbons, Additive layer manufacture of Inconel 625 metal matrix composites, reinforcement material evaluation, J. Mater. Process Technol. 213 (2013) 2191–2200, https://doi.org/10.1016/J.JMATPROTEC.2013.06.021.

[43] Y.L. Wang, L. Zhao, D. Wan, S. Guan, K.C. Chan, Additive manufacturing of TiB2-containing CoCrFeMnNi high-entropy alloy matrix composites with high density and enhanced mechanical properties, Mater. Sci. Eng.: A 825 (2021), 141871, https://doi.org/10.1016/J.MSEA.2021.141871.

[44] D. Gu, H. Zhang, D. Dai, M. Xia, C. Hong, R. Poprawe, Laser additive manufacturing of nano-TiC reinforced Ni-based nanocomposites with tailored microstructure and performance, Compos B Eng. 163 (2019) 585–597, https://doi.org/10.1016/J.COMPOSITESB.2018.12.146.

[45] J. Li, H. Qu, J. Bai, Grain boundary engineering during the laser powder bed fusion of TiC/316L stainless steel composites: New mechanism for forming TiC-induced special grain boundaries, Acta Mater. 226 (2022), 117605, https://doi.org/10.1016/j.actamat.2021.117605.

[46] Y. Xiang, S. Zhang, Z. Wei, J. Li, P. Wei, Z. Chen, L. Yang, L. Jiang, Forming and defect analysis for single track scanning in selective laser melting of Ti6Al4V, Applied Physics A. 124 (2056) 685. https://doi.org/10.1007/s00339–018-2056–9.

[47] A.S. Hakeem, F. Patel, N. Minhas, A. Malkawi, Z. Aleid, M.A. Ehsan, H. Sharrofna, A. al Ghanim, Comparative evaluation of thermal and mechanical properties of nickel alloy 718 prepared using selective laser melting, spark plasma sintering, and casting methods, J. Mater. Res. Technol. 12 (2021) 870–881, https://doi.org/10.1016/J.JMRT.2021.03.043.

[48] M. Tanjilul, A. Ahmed, A.S. Kumar, M. Rahman, A study on EDM debris particle size and flushing mechanism for efficient debris removal in EDM-drilling of Inconel 718, J. Mater. Process Technol. 255 (2018) 263–274, https://doi.org/10.1016/J.JMATPROTEC.2017.12.016.

[49] A. Maity, D. Kalita, T.K. Kayal, T. Goswami, O. Chakrabarti, H.S. Maiti, P.G. Rao, Synthesis of SiC ceramics from processed cellulosic bio-precursor, Ceram. Int 36 (2010) 323–331, https://doi.org/10.1016/J.CERAMINT.2009.09.006.

[50] E. Zapata-Solvas, S. Bonilla, P.R. Wilshaw, R.I. Todd, Preliminary investigation of flash sintering of SiC, J. Eur. Ceram. Soc. 33 (2013) 2811–2816, https://doi.org/10.1016/J.JEURCERAMSOC.2013.04.023.

[51] B. Zhang, P. Wang, Y. Chew, Y. Wen, M. Zhang, P. Wang, G. Bi, J. Wei, Mechanical properties and microstructure evolution of selective laser melting Inconel 718 along building direction and sectional dimension, Mater. Sci. Eng.: A 794 (2020), 139941, https://doi.org/10.1016/J.MSEA.2020.139941.

[52] Z. Song, W. Gao, D. Wang, Z. Wu, M. Yan, L. Huang, X. Zhang, F. Mazzucato, materials Very-High-Cycle Fatigue Behavior of Inconel 718 Alloy Fabricated by Selective Laser Melting at Elevated Temperature, 2021. https://doi.org/10.3390/ma14041001.

[53] X.Y. Fang, H.Q. Li, M. Wang, C. Li, Y.B. Guo, Characterization of texture and grain boundary character distributions of selective laser melted Inconel 625 alloy, Mater. Charact. 143 (2018) 182–190, https://doi.org/10.1016/J.MATCHAR.2018.02.008.

[54] H. Yu, S. Hayashi, K. Kakehi, Y.L. Kuo, Study of formed oxides in IN718 alloy during the fabrication by selective laser melting and electron beam melting, Met. (Basel) 9 (2019), https://doi.org/10.3390/met9010019.

[55] L.Y. Sheng, Y.X. Tian, J.T. Guo, Microstructural Characteristics and Mechanical Properties of a Nb/Nb5Si3 based Composite with and without Directional Solidification, Adv. Compos. Lett. 27 (2018), https://doi.org/10.1177/096369351802700405.

[56] Y. Zhou, A. Volek, Effect of carbon additions on hot tearing of a second generation nickel-base superalloy, Mater. Sci. Eng.: A 479 (2008) 324–332, https://doi.org/10.1016/J.MSEA.2007.06.076.

[57] Z. Sun, Y. Ma, D. Ponge, S. Zaefferer, E.A. Jägle, B. Gault, A.D. Rollett, D. Raabe, Thermodynamics-guided alloy and process design for additive manufacturing, Nat. Commun. 13 (2022) 4361, https://doi.org/10.1038/s41467-022-31969-y.

[58] F. Vakili-Tahami, M.R. Adibeig, Investigating the possibility of replacing IN 738LC gas turbine blades with IN 718 †, J. Mech. Sci. Technol. 29 (2015) 4167–4178, https://doi.org/10.1007/s12206-015-0911-6.

[59] F.R. Caliari, K.C.G. Candioto, D.A.P. Reis, A.A. Couto, C. de Moura Neto, C. A. Nunes, Study of the Mechanical Behavior of an Inconel 718 Aged Superalloy Submitted to Hot Tensile Tests, SAE Technical Papers,, 2011, https://doi.org/10.4271/2011-36-0328.

[60] T.-H. Hsu, K.-C. Chang, Y.-J. Chang, I.-T. Ho, S. Tin, C.-W. Li, K. Kakehi, C.-P. Chen, K.-K. Jen, H.-Y. Hsieh, A.-C. Yeh, in: S. Tin, M. Hardy, J. Clews, J. Cormier, Q. Feng, J. Marcin, C. O'Brien, A. Suzuki (Eds.), Effect of Carbide Inoculants Additions in IN718 Fabricated by Selective Laser Melting Process, Superalloys 2020, Springer International Publishing, Cham, 2020, pp. 982–989.

[61] W.Z. Zheng, X. Wie, Z. Song, Q. Yong, H. Feng, Q. Xie, Effects of Carbon Content on Mechanical Properties of Inconel 718 Alloy, J. Iron Steel Res. Int. 22 (2015) 78–83, https://doi.org/10.1016/S1006-706X(15)60013-9.Effects of Carbon Content on Mechanical Properties of Inconel 718 Alloy, n.d. www.sciencedirect.com (accessed October 31, 2022).

[62] Q.S. Song, Y. Zhang, Y.-F. Wei, X.-Y. Zhou, Y.-F. Shen, Y.-M. Zhou, X.-M. Feng, Microstructure and mechanical performance of ODS superalloys manufactured by selective laser melting, Opt. Laser Technol. 144 (2021), 107423, https://doi.org/10.1016/J.OPTLASTEC.2021.107423.